Precise seismic-wave velocity atop Earth's core:

No evidence for outer-core stratification

Authors: Catherine Alexandrakis[*a] and David W. Eaton[b]

University of Calgary, Department of Geoscience, 2500 University Drive NW, Calgary, Alberta, Canada T2N 1N4

[a] alexanc@ucalgary.ca [b] eatond@ucalgary.ca

Physics of the Earth and Planetary Interiors 180 (2010) 59–65

Keywords

core, velocity model, *SmKS* phase, empirical transfer function, whispering-gallery mode

Abstract

Earth's outer core is composed of liquid Fe and Ni alloyed with a ~ 10% fraction of light elements such as O, S, or Si. Secular cooling and compositional buoyancy drive vigorous convection that sustains the geodynamo, but critical details of light-element composition and thermal regime remain uncertain. Seismic velocities can provide important observational constraints on these parameters, but global reference models such as Preliminary Reference Earth Model (*PREM*), *IASP91* and *AK135* exhibit significant discrepancies in the outermost ~ 200 km of the core. Here, we apply an Empirical Transfer Function method to obtain precise arrival times for *SmKS* waves, a whispering-gallery mode that propagates near the underside of the core-mantle boundary. Models that fit our data are all characterized by seismic velocities and depth gradients in the outermost 200 km of the core that correspond best with *PREM*. This similarity to *PREM*, which has a smooth velocity profile that satisfies the adiabatic Adams and Williamson equation, argues against the presence of an anomalous layer of light material near the top of the core as suggested in some previous studies. A new model, *AE09*, is proposed as a slight modification to *PREM* for use as a reference model of the outermost core.

1.0 Introduction

In recent years, seismological, geodynamic and mineral-physics studies have elucidated complexities that exist within the core-mantle boundary (CMB) region. Some outer-core studies predict unusual features in this region, such as sediment accumulation (Buffett et al., 2000), immiscible fluid layers (Helffrich and Kaneshima, 2004) or stagnant convection (Lister and Buffett, 1998; Lay et al., 2008). Improved knowledge of the composition and structure of the outermost core should lead to a better understanding of the geodynamo, conditions of inner-core growth and core-mantle interactions (Lay et al., 2008). Seismic velocity models can also help to constrain estimates of core composition and structure. Global reference models, such as Preliminary Reference Earth Model (*PREM;* Dziewonski and Anderson, 1981), *IASP91* (Kennett and Engdahl, 1991) and *AK135* (Kennett et al., 1995) were created with different data sets, techniques and assumptions, leading to differences in some regions of Earth. In particular, these models show significant variability in a ~200 km depth range immediately below the CMB, adding uncertainty to our understanding of this region.

The most direct measure of seismic velocity of the outermost core region is provided by *SmKS* waves, which travel as *S*-waves in the mantle and *P*-waves in the core, with *m*-1 underside bounces at the CMB (Fig. 1). At epicentral distances of 115-140^{o} the arrival times and amplitudes of *SmKS* arrivals are highly sensitive to the velocity structure of the outermost core (Choy, 1977), especially near their turning depths, which become progressively shallower as m increases. This region of sensitivity generally coincides with the depth-region of the outer core where current global velocity models exhibit the largest discrepancies (Helffrich and Kaneshima, 2004; Eaton and Kendall, 2006). Within this distance range, *SKS* and *SKKS* are typically observed as distinct phases in broadband seismograms, whereas higher-order *SmKS* modes (m > 2) coalesce into a dispersive wavetrain that propagates near the top of the core (Choy, 1977; Eaton and Kendall, 2006). Depending on the observation distance and the signal-to-noise ratio, *S3KS* and *S4KS* phases may be identified as distinct arrivals within the wavetrain. This composite pulse constitutes a whispering-gallery mode, analogous to acoustic modes that propagate

within the domes of large cathedrals (Aki and Richards, 2002).

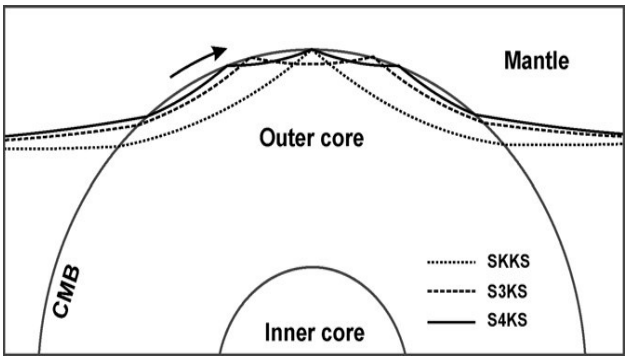

Figure. 1. SmKS ray paths. SmKS rays travel as S waves in the mantle and P waves in the core where they reflect m−1 times off of the core side of the CMB. For epicentral distances from 115–140°, SmKS waves (m> 2) coalesce to form a whispering-gallery mode (Aki and Richards, 2002).

In principle, arrival times for any distinct *SmKS* phase may be inverted directly using the Herglotz-Wiechert (H-W) formula to obtain seismic velocity above the turning depth (Hales and Roberts, 1971). In practice this approach is unreliable, in part due to the limitation of the H-W approach to monotonic increasing velocity functions but largely because *SmKS* phases can be strongly perturbed by velocity heterogeneities above the core, particularly in the case of strong lateral variations in the *D*″ region (Garnero and Helmberger, 1995; Tanaka, 2004). To mitigate this uncertainty, seismologists measure differential times between successive *SmKS* phases (typically *S3KS-SKKS*). This approach provides nearly complete cancellation of traveltime perturbations due to the similarity in mantle paths of the respective phases (Souriau and Poupinet, 1991; Garnero et al., 1993). Nevertheless, compilations of *SmKS* differential time measurements contain significant scatter, limiting resolution of detailed velocity structure of the outermost part of the core (Souriau and Poupinet, 1991; Souriau et al., 2003; Eaton and Kendall, 2006).

Here, we use the Empirical Transfer Function (ETF) technique (Alexandrakis and Eaton, 2007, herein AE2007) to facilitate stacking of broadband *SmKS* waveforms. The ETF method removes the earthquake source pulse using Wiener deconvolution, in a manner similar to teleseismic receiver functions (e.g., Langston, 1979). Like receiver functions, time picks for distinctive ETF waveform elements provide robust proxies for the differential traveltimes of *SmKS* phases. Since *SmKS* waves pass through a caustic at the turning point in each core leg, the pulse shape associated with a specific arrival is related to the pulse shape of the previous arrival by a Hilbert transform (neglecting phase changes at the underside bounce point; see Choy, 1977). Consequently, as demonstrated previously (AE2007), the arrival time of a zero-crossing provides a proxy for the *S3KS-SKKS* differential time, whereas the *S4KS-SKKS* differential is represented by the following trough (Fig. 2). Only *S3KS* arrivals were measured in our initial study (AE2007); here, we apply the same approach to a larger dataset, consider *S4KS-SKKS* differential traveltimes, and perform a more comprehensive search for optimal velocity structure. We remark that *S4KS-S3KS* differential times could be computed using the ETF method, with *S3KS* as a reference phase; however, this extra step would not provide any additional information, since *S4KS-S3KS* differential times can be obtained by subtraction of the *S3KS-SKKS* from the *S4KS-SKKS* measurements.

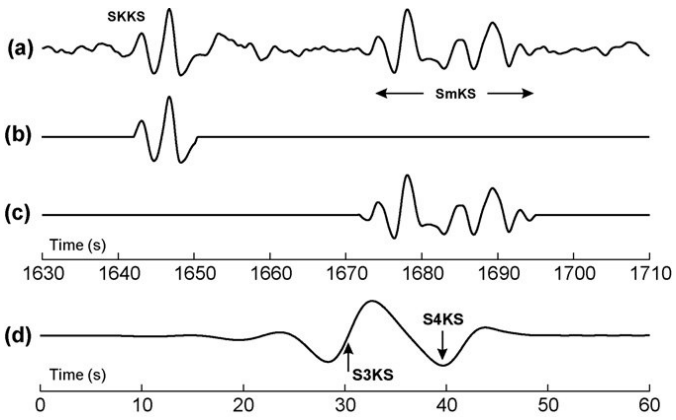

Figure. 2. ETF Example. (a) Sample observed trace from 2004-07-25 Sumatran deepfocus earthquake (z = 582.1 km) recorded at station PLIO (see supplementary data). SKKS and SmKS phases are indicated. (b) Time-windowed SKKS phase. (c) Timewindowed SmKS phase. (d) Resultant ETF, obtained by Wiener deconvolution. At this distance (140.39°), S3KS and S4KS phases are resolved within the SmKS wavetrain. Differential traveltimes are indicated at the zero-crossing (S3KS–SKKS) and trough (S4KS–SKKS).

2.0 *SmKS* Record Section

The Empirical Transfer Function (ETF) method reduces the scatter in traveltime measurements via a deconvolution procedure that normalizes the source pulse, which varies between events (AE2007). This approach facilitates stacking of broadband *SmKS* waveforms, thus effectively averaging-out lower-mantle heterogeneity and yielding more accurate differential time calculations. Like receiver functions (Langston 1979), the time axis of ETF waveforms represents differential time relative to the reference phase, which for this application is the *SKKS* arrival.

We have compiled 707 *SmKS* arrivals from teleseismic earthquakes with a variety of source depths, yielding 1414 differential phase measurements (see supplementary data). The observations come from 44 individual earthquakes of magnitude 6 or greater. Aftershocks are used in some cases, but do not increase the total number of events since no new raypath data is obtained. The events vary in focal depth and include 8 shallow (< 70 km depth), 9 intermediate (between 70 and 300 km deep) and 27 deep-focus (> 300 km depth) earthquakes. The corresponding CMB entry and exit points sample a wide range of conditions in the lowermost mantle (Fig. 3a). In particular, the *S*-wave velocity difference between *SKKS* and *S4KS* entry and exit points has a mean value close to zero (Fig. 3b), indicating that the stacking process used here tends to cancel velocity differences in the lower mantle. Moreover, our dataset densely samples the outermost part of the core, with 95% of the *S3KS* and *S4KS* turning depths between 60 and 200 km below the CMB.

The observed data were filtered with a 4th order Butterworth filter with corner frequencies of 0.05 Hz and 1.0 Hz. Instrument response, trend and mean were removed prior to calculating the ETF using the method described by AE2007. In brief, a time-domain windowing function is used to isolate the reference (*SKKS*) and target (*SmKS*) phases, after which the least-squares transfer function is computed by Wiener deconvolution (Fig. 2). After calculating the ETF waveform, we apply a Gaussian filter with a standard deviation of 0.15 Hz. The calculated and filtered ETFs were corrected for Earth's ellipticity (Kennett and Gudmundsson, 1996) by calculating the applicable phase-specific correction (e.g., *SKKS, S4KS*) and determining a time-dependent stretch factor, which was then applied to the ETF waveform by cubic-spline interpolation. Ellipticity-corrected ETF

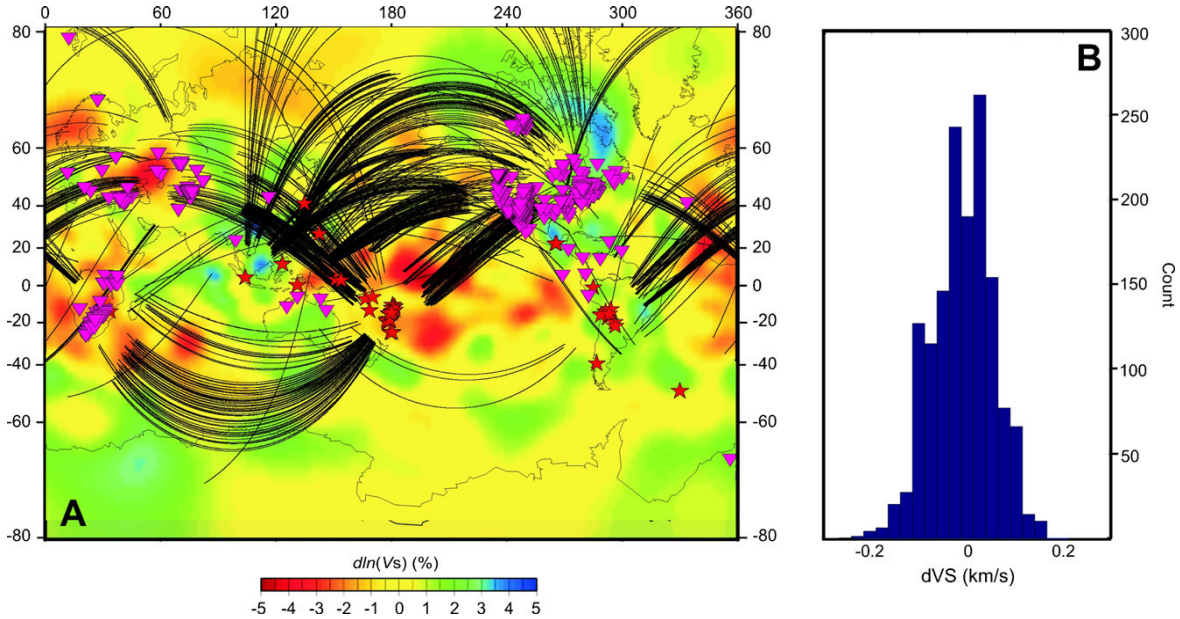

Figure. 3. SmKS ray paths, distribution and CMB sampling. (a) Epicenters (stars), stations (triangles) and core segment of SmKS ray paths, superimposed on a map of lowermost mantle shear-wave velocity at 2850km depth, from model SAW24B16 (Mégnin and Romanowicz, 2000). End points of arcs indicate SKKS entry and exit points from the core. Blue and red regions represent high and low velocities, respectively. (b) Histogram of velocity difference (mean −0.009 km/s) between SKKS and S4KS piercing points at the core–mantle boundary. The nearly symmetrical distribution around zero implies that, for this ray coverage, the stacking procedure used here will tend to average out time shifts caused by lowermost mantle heterogeneity (Garnero et al., 1993).

waveforms were sorted by *SKKS* slowness parameter, and stacked in bins 0.025 degrees/second in size. Bins with 6 or fewer traces were discarded, resulting in a loss of 10 traces, or 1.4% of the total dataset. The resulting stacked broadband ETF section (Fig. 4) reveals the *S3KS* and *S4KS* branches of *SmKS* with unusual clarity. The inclusion of *S4KS* observations in this study significantly increases the number of observations in the outermost core.

Using a semi-automated picking algorithm, *S3KS* and *S4KS* arrival times relative to *SKKS* were extracted from the stacked ETF record section. Traveltime (moveout) curves were then fit to these measurements following the procedure of AE2007. The moveout curves are obtained by subtracting the differential times computed using a reference model, fitting a linear trend to the residuals, then summing of the linear trend and the reference times. Here we used *PREM* for a reference model, for consistency with AE07, but we have verified by testing that the moveout curves are insensitive to the choice of reference model (i.e., the resulting moveout curves are negligibly different). *S3KS-SKKS* and *S4KS-SKKS* differential time picks for each bin, and the calculated moveout curve values are given in Table 1.

The scatter around the empirical moveout curves (Fig. 4 inset) for these *SmKS* branches was quantified by averaging the root-mean-squared (RMS) error between the observations and moveout curves. For this stack, the RMS scatter is 0.51s, significantly less than the scatter in differential traveltimes from previous outer core studies (e.g., Souriau and Poupinet, 1991; Garnero et al., 1993; Eaton and Kendall, 2006). Bootstrap analysis (Chernick, 1999) was used to define 98% confidence limits for the moveout curves (Fig. 4 inset), where bins were restacked 10 000 times using random substitution. The uncertainties in the moveout curves determined this way are significantly smaller than the scatter in the observed data.

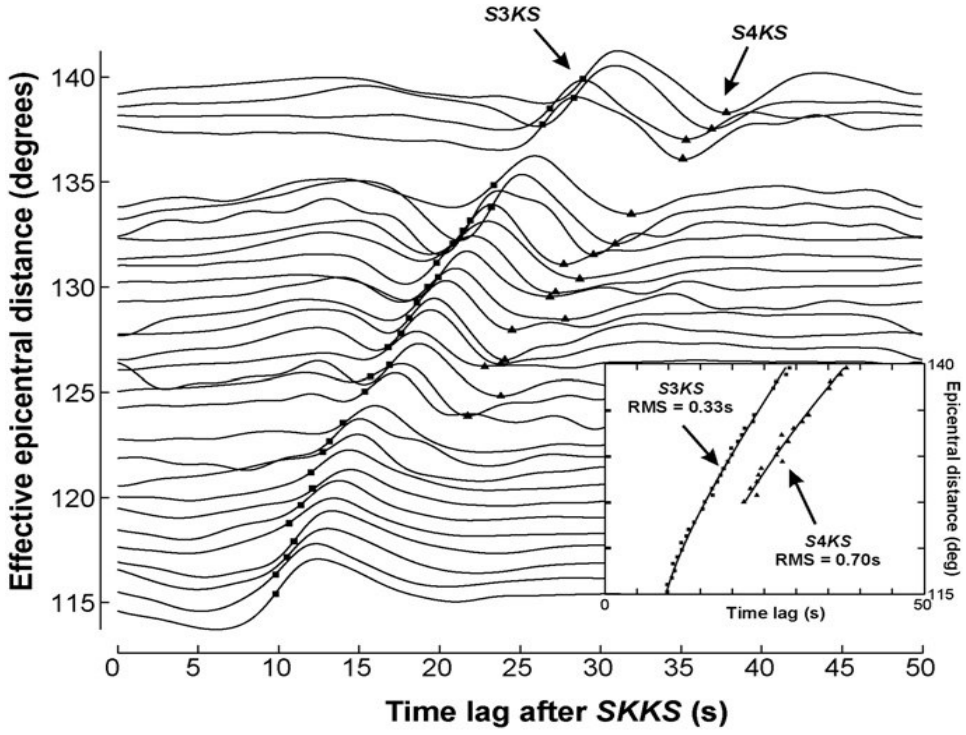

Figure. 4. Stacked empirical transfer function (ETF) profile. Epicentral distance is computed for a reference focal depth of 500 km. Symbols indicate arrival-time picks (snapped to waveforms) for S3KS and S4KS phases, relative to SKKS. Inset shows the fit of the derived moveout curves to these picks, along with the corresponding rootmean- squared (RMS) scatter for each phase. Errorbars are very small and indicate 98% confidence limits based on bootstrap resampling.

3.0 Modeling and Inversion

SmKS traveltimes are exceptionally sensitive to velocity structure of the outermost core, particularly the *S4KS* branch that has not previously been well imaged by broadband seismic observations in the shallow-turning epicentral distance range of 124-140°. Here, we investigate a large suite of velocity models by measuring differential times using the ETF method applied to synthetic seismograms. The reflectivity method with Earth flattening correction (Fuchs and Müller, 1971) was used to compute synthetic seismograms, since this method includes the complete (infinite) sequence of multiple reflections in the whispering-gallery waveform and accounts for finite-frequency effects (Choy, 1977). Model layers were 50 km thick in most regions of Earth, but 10 km thick in the outermost 200 km of the outer core. Throughout the outer core, we use a high Q_p value (10 000).

Table 1. Observed picks and moveout curve values. Picked *S3KS-SKKS* and *S4KS-SKKS* differential times for each slowness bin and the corresponding epicentral for an equivalent 500 km depth focus earthquake. Calculated moveout curves for the *S3KS* and *S4KS* branches are also given.

Slowness	Delta	Δt S3KS–SKKS	S3KS–SKKS Moveout curve	Δt S4KS–SKKS	S4KS–SKKS Moveout curve
5.8620	139.5739	28.90	28.5734	37.80	37.7487
5.8860	138.8493	28.35	27.8514	36.90	36.8390
5.9090	138.1246	26.90	27.1384	35.30	35.9427
5.9350	137.4000	26.40	26.4350	35.10	35.0605
6.0100	135.2261	25.25	24.3726	34.20	32.4823
6.0350	134.5014	23.40	23.7031	31.90	31.6488
6.0590	133.7768	23.20	23.0410	30.90	30.8262
6.0850	133.0522	21.90	22.3874	29.55	30.0154
6.1110	132.3275	21.45	21.7447	27.70	29.2205
6.1370	131.6029	20.85	21.1097	28.70	28.4364
6.1620	130.8783	19.85	20.4822	27.20	27.6630
6.1860	130.1536	19.90	19.8649	26.85	26.9040
6.2100	129.4236	19.25	19.2529	27.80	26.1533
6.2350	128.6922	18.60	18.6476	24.50	25.4123
6.2610	127.9608	18.10	18.0502	24.05	24.6823
6.2870	127.2294	17.60	17.4647	23.80	23.9691
6.3110	126.4980	16.80	16.8878	22.80	23.2678
6.3350	125.7665	16.85	16.3188	23.80	22.5776
6.3600	125.0351	15.75	15.7586	–	–
6.3860	124.2938	15.40	15.2032	–	–
6.4370	122.8101	14.00	14.1169	–	–
6.4610	122.0682	13.15	13.5875	–	–
6.4860	121.3264	12.80	13.0702	–	–
6.5100	120.5846	12.05	12.5613	–	–
6.5350	119.8380	12.05	12.0576	–	–
6.5610	119.0740	11.35	11.5528	–	–
6.5870	118.3099	10.70	11.0602	–	–
6.6120	117.5458	10.90	10.5769	–	–
6.6360	116.7818	10.50	10.1030	–	–
6.6600	116.0177	9.80	9.6386	–	–
6.6850	115.2537	9.80	9.1873	–	–

The synthetic seismograms were subsequently processed using the ETF method described above. For each candidate velocity model, misfit was determined by computing the RMS time difference between modeled *S3KS-SKKS* and *S4KS-SKKS* differential times relative to the smooth moveout curves determined from our data. Automatic picks were inspected to remove any spurious values arising from numerical artifacts in the reflectivity modeling process. The moveout curves were used as the basis for measuring goodness of fit, rather than the observed differential times, to reduce the effects of scatter in the measurements since any realistic Earth model yields smoothly varying differential traveltimes. Based on this approach, a model is deemed admissible if it yields a mean RMS time difference that is less than or equal to the mean RMS scatter of the observed data. As elaborated below, of the standard Earth models *PREM, IASP91* and *AK135*, only *PREM* satisfies this criterion.

To augment the range of models considered, a suite of hybrid velocity models were derived using linear combinations of *PREM, IASP91* and *AK135* specified in 10% increments. In addition, to evaluate a wider range of top-of-core velocities and gradients, perturbations to these hybrid models were applied within the outermost 200 km of the core, the depth interval where these reference models show the greatest degree of variability (Eaton and Kendall, 2006). Each perturbed model is parameterized according to a top-of-core velocity, V_0, and a perturbation thickness h (= 20, 50, 100,150 or 200 km).

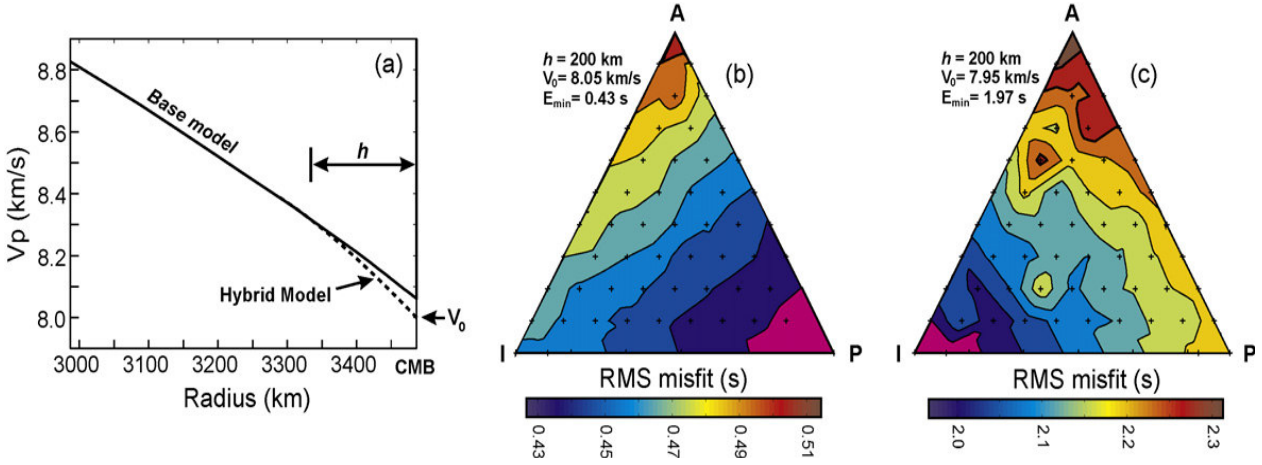

Figure 5. **Modeling and inversion method**. **(A)** A hybrid model is constructed using a linear combination of standard Earth models *AK135* (Kennett et al., 1995), *IASP91* (Kennett and Engdahl, 1991) and *PREM* (Dziewonski and Anderson, 1981). It is then perturbed by inserting a layer of thickness h with P-wave velocity V_0 at the core-mantle boundary (CMB). This layer has quadratic velocity dependence with respect to radius, and matches the hybrid model and its first derivative at depth h below the CMB. **(B)** Misfit values for one set of perturbed models, presented as a ternary diagram. . *A*, *I* and *P* denote V_0 values for *AK135*, *IASP91* and *PREM*, respectively. Minimum misfit is denoted as E_{min}. **(C)** As in (B), for V_0 = 7.95 km/s. Note change in scale for misfit.

We sampled V_0 every 0.05 km/s in the range from 7.7 to 8.15 km/s. In the range of 7.95-8.1 km/s, we sampled every 0.025 km/s and also tested 8.01 and 8.09 km/s. We evaluated various functional forms for the perturbation models and found that models with quadratic depth dependence,

$$V(r) = V_0 + a(r - r_{CMB}) + b(r - r_{CMB})^2 \quad , r_{CMB} - h \le r \le r_{CMB} \quad , \qquad (1)$$

yield synthetic seismograms very similar to the observed data, where r is the radius and r_{cmb} is the radius at the core-mantle boundary. Model coefficients a and b are chosen so that $V(r)$ merges smoothly with the corresponding hybrid velocity model at depth h below the CMB (Fig. 5a), i.e., velocity and its depth derivative are both continuous at h. Above the CMB, most models are standardized to the velocity structure of *AK135*, since this is the global reference model that provides the best fit to teleseismic observations of mantle waves (Kennett et al., 1995).

Ternary contour diagrams of the RMS misfit (Fig. 5b and c) show that the best-fitting models tend towards solutions with a high proportion of *IASP91* or *PREM*. Of 1458 models tested with an *AK135* mantle, the best fit was obtained for a core hybrid model of 20% *IASP91* and 80% *PREM*, where V_0 = 8.05 km/s and h = 150 km (Table 2). The quadratic parameters a and b (Equation 1) for the outer 200 km of Earth's core for this model are -1.7701 s^{-1} and -5.2813 x 10^{-7} $km^{-1}s^{-1}$, respectively. Our best-fitting model, herein referred to as *AE09*, yields a 30% reduction in RMS misfit (0.36 s) compared to the RMS misfit for *PREM* (0.51 s). The misfit reduction results mainly from a slight lowering of V_0 from 8.064 km/s (Dziewonski and Anderson, 1981) to 8.05 km/s.

4.0 Seismic velocity at the top of the core

Model misfit is plotted as a function of V_0 in Figure 6. For each value of V_0, this graph shows the best fit for all hybrid models and values of h. Since our suite of hybrid models is derived from blends of *PREM*, *IASP91* and *AK135*, the minimum misfit for V_0 = 8.05±0.03 km/s may be regarded as independent of the particular core velocity structure in any of these global reference models. The flat shape of the minimum region reflects tradeoffs that occur between V_0 and other model parameters (i.e. hybrid model and layer thickness). As a further test to determine the possible sensitivity of V_0 to 1-D mantle model, a suite of models was prepared with a *PREM* mantle and an *IASP91* mantle adjusted to fit the core radius for *AK135*. Below 150 km depth beneath the CMB, we use the hybrid model of *AE09* and vary V_0 (7.7 – 8.16 km/s). The models that fell within the acceptable RMS misfit range all had V_0 values within the inferred accepted range and centered on V_0 = 8.05 km/s (Fig. 6).

Table 2. Model *AE09*. Radius, *P* wave velocity (α) and density (ρ) values for the upper 200 km of the outer core. Density is calculated according to the Adams and Williamson equation (1). Core-mantle boundary radius is selected to correspond with *AK135*.

Radius (km)	α (km/s)	ρ (Mg/m^3)
3479.5	8.0500	9.901
3469.9	8.0669	9.917
3460.4	8.0840	9.932
3450.8	8.1010	9.947
3441.2	8.1169	9.963
3431.7	8.1341	9.978
3421.6	8.1510	9.994
3411.5	8.1679	10.010
3401.5	8.1850	10.026
3391.4	8.2020	10.042
3381.3	8.2189	10.057
3371.3	8.2360	10.073
3361.2	8.2520	10.089
3351.1	8.2689	10.104
3341.1	8.2850	10.119
3320.9	8.3010	10.135
3310.9	8.3169	10.150
3300.8	8.3340	10.165
3290.7	8.3500	10.180
3280.7	8.3659	10.196

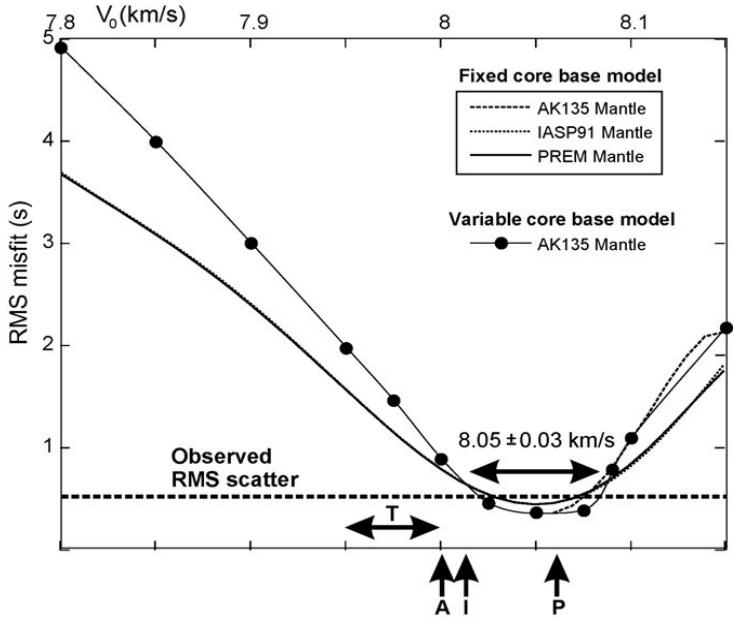

Figure 6. Misfit function. For each value of V_0 the minimum misfit for all corresponding hybrid models with a mantle of *AK135* (solid line with dots). Solid, dotted and dashed lines denote *PREM*, *IASP91* and *AK135* mantle models, respectively, with a base model of *AE09*. Models with misfit less than the observed scatter (0.51 s, bold dashed line) are deemed admissible. *A*, *I* and *P* denote V_0 values for *AK135*, *IASP91* and *PREM*, respectively. *T* is V_0 range from Tanaka (2007).

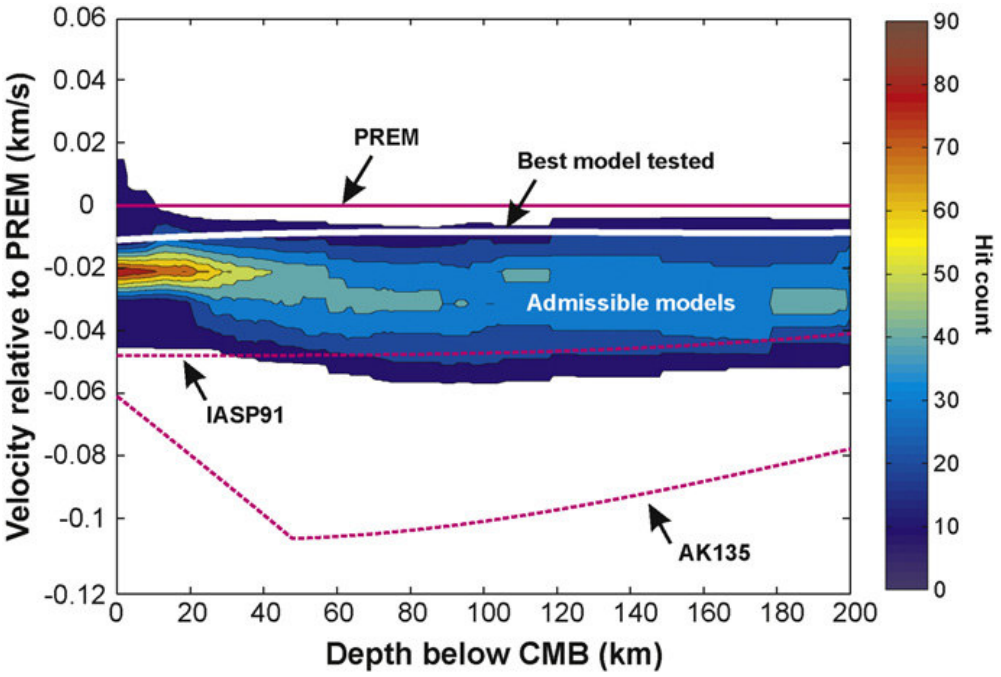

Figure 7. Velocity models in the outermost core, plotted with respect to *PREM*. Admissible models (contoured region) are generally intermediate in velocity between *IASP91* (Kennett and Engdahl, 1991) and *PREM* (Dziewonski and Anderson, 1998). The best model tested has velocity 8.05 km/s at the core-mantle boundary (CMB) and perturbation thickness 150 km, with a velocity gradient very similar to *PREM*. Model *AK135* (Kennett et al., 1995) shows significantly lower velocity in the outermost core. Contours indicate hit count of the admissible velocity models for bins sized 0.01km/s by 1 km sized bins.

The inferred range of top-of-outer core velocities includes a velocity of 8.04 km/s that was proposed by AE2007 by fitting only *S3KS-SKKS* differential arrival times, but excludes the range of 7.95 – 8.0 km/s defined by Tanaka (2007), based on a long-period stack of *SmKS* waves. This discrepancy may reflect the higher resolution of our broadband stack; for example, the *S4KS-SKKS* differential time at shallow turning depths, required to constrain the velocity model near the top of the core, is considerably less than the dominant period in Tanaka (2007). In the case of long-period data, waveform interference will strongly influence the arrival-time picks.

The range of admissible models is summarized in Figure 7. The shaded and contoured region in Figure 7 represents the density ('hit count') of admissible models per 1 km x 0.01 km/s bin. Interestingly, the model with the smallest RMS error does not lie in the middle of this region, perhaps reflecting an asymmetric RMS error distribution within the range of admissible models. In general, admissible models are intermediate in velocity between *IASP91* and *PREM*. In addition, velocity gradients near the top of the core for all admissible models strongly resemble *PREM*. Given that model *AK135* provides a better statistical fit to most global seismic observations than these older models (Kennett et al., 1995), it is surprising that it contains significantly lower-than-admissible velocities in the outermost core region. In particular, robust traveltime observations for *PKP* and *PKIKP* waves, which are easy to detect and measure, are better explained by *AK135* than other global reference models (Kennett et al., 1995).

To explore the sensitivity of these other core phases to our proposed velocity structure, we performed a series of tests using computed arrival times for *PKP* and *PKIKP* waves. As *AE09* is confined to the outermost 200 km of the core, two models were considered. The first model uses *AE09* with its hybrid velocity model in the remainder of the outer core (i.e., a weighted combination of *PREM* and *IASP91*) and *AK135* in the inner core. The second scenario perturbs model *AK135* by adjusting the top of core velocity to fit the inferred best value (8.05 km/s), with a smooth 200 km transition to

the deeper *AK135* core velocity structure. A 500 km source depth was used throughout. Using Taup ToolKit (Crotwell et al., 1999), we calculated the mean RMS error value for *PKP* (8.165×10^{-3} s and 1.2484 s for case 1 and case 2, respectively) and *PKIKP* (2.774×10^{-3} s and 0.6442 s for case 1 and case 2, respectively) and found that the traveltime differences that arise from both perturbation scenarios are less than the standard deviations of observed traveltimes used to construct *AK135*. We conclude, therefore, that our proposed velocity structure at the top of the core is compatible, to within the uncertainty, with the kinematic properties of these other core phases.

5.0 Density and Moment of Inertia

Under the assumptions that conditions in the outer core are homogeneous and adiabatic, the density and seismic velocity are governed by the Adams and Williamson equation (Williamson and Adams, 1923; Poirier, 2000)

$$\frac{d\rho}{dr} = -g\rho\Phi_S^{-1} \quad , \tag{2}$$

where r is radius from the centre of the Earth, $\rho(r)$ is density, $g(r)$ is the acceleration of gravity and $\Phi_S = v_p^2$ is called the seismic parameter. We assigned velocity values from *AE09* into the outer core of global model *AK135* and solved equation (2) using an iterative approach to estimate the corresponding densities in the outermost 200 km (Table 2). For each iteration, we calculated Earth's mass

$$M = 4\pi \int_0^{R_E} r^2 \rho dr \tag{3}$$

and gravity profile

$$g = \frac{GM}{r^2} \quad , \tag{4}$$

where R_E is Earth's radius (6371 km) and $G = 6.6627 \times 10^{-11}$ $m^3 kg^{-1} s^{-2}$ is the Universal Gravitational constant. An updated density profile was calculated by integrating equation (2) over the outer core radii (1221.5 – 3479.5 km) to give

$$\rho = \rho_o e^{\int_{r_{ICB}}^{r_{CMB}} \frac{g}{\Phi_S} dr} \tag{5}$$

using the calculated core gravity profile, g, velocity models *AE09* in the outer core and *AK135* in the inner core to define Φ_S, and *PREM*'s density at the CMB for ρ_o (9.901 Mg/m^3). The new core densities are used to update the global density profile. This procedure was iterated until convergence to a self-consistent density-gravity model was achieved, generally less than 10 iterations. This model is self-consistent but not unique – it depends on the assumed value of ρ_o. We remark that the radius at the CMB, r_{CMB} and at the Inner Core Boundary (ICB), r_{ICB} are adopted from *AK135*. From one global model to the next, the radius to the CMB and ICB differs by a few kilometers; these differences are minor and do not significantly affect the results.

Since *PREM* fits the Earth's mass (M) and moment of inertia ratio (I), we tested this model to verify that the perturbed values are compatible with our knowledge of these parameters. Earth's moment of inertia (η) is given by

$$\eta = 4\pi \frac{2}{3} \int_0^{R_E} r^4 \rho dr \quad . \tag{5}$$

This can also be expressed in terms of Earth's mass, M = 5.9736×10^{24} kg and moment of inertia ratio, I = 0.3307144 (Kennett, 1998) using

$$\eta = IMr^2 \quad . \tag{6}$$

Relative to *PREM*, we obtained $\Delta M = 1.75 \times 10^{20}$ kg and $\Delta I = 1.08 \times 10^{-5}$, both of which are significantly less than their respective uncertainties (Kennett, 1998). We conclude, therefore, that model *AE09* is compatible with known values of Earth's moment of inertia and gravity.

6.0 Discussion

As noted above, a number of previous authors have hypothesized the existence of fine layers at the top of the core. For example, Helffrich and Kaneshima (2004) investigated the possibility of a light-element enriched immiscible fluid layer at the top of the outer core. Using a thermodynamic approach within the Fe-O-S system, they obtained a range of density and incompressibility values for core fluids that fit *PREM*, and showed that some permissible scenarios predict a light-element enriched immiscible fluid that would accumulate at the top of the core. They noted a lack of precursory phases to *PmKP* events, however, which suggested that such a layer is unlikely to exist. Several other studies have proposed a stably stratified layer at the top of the outer core, which can only exist if the outer core is subadiabatic (Lister and Buffett, 1998; Lay et al. 2008). Lister and Buffett (1998) estimated that such a layer would have a thickness of approximately 100 km, which would be easily detectible using our method. However, the clustering of admissible models in our study close to *PREM* strongly

suggests that well mixed, adiabatic conditions prevail in the outermost core region.

Buffett et al. (2000) hypothesized that Si enriched sediments may have been deposited at the top of the core since its initial formation. According to this model, sediments may have accumulated within topographically elevated regions of the CMB and are expressed in seismic velocity models as ultra low-velocity zones (ULVZs) in the lowermost mantle. If the accommodation space in these elevated regions is insufficient to hold the entire volume of material, a thin layer of Si enriched sediments could exist around the entire top surface of the outer core. Since outside of ULVZs such a layer could be too thin to resolve using the ETF technique, we cannot rule out this possibility.

Velocity models of the outer core provide useful constraints for light-element composition. Although newer global models including *IASP91* and *AK135* provide a better overall fit to seismic observations, *PREM* is still commonly invoked as a seismological constraint for the validation of mineral physics experimental data and for interpretation of *ab initio* molecular dynamics simulations (e.g., Koci et al., 2007). For example, Si has been found to be a strong candidate light element based on *PREM*'s velocity profile (Sanloup et al., 2004; Morard et al., 2008) and incompressibility (Sanloup et al., 2004). Given the similarity of *AE09* to *PREM*, the results of our study provide support for the continued use of *PREM* as a reference model for the outermost 200 km of the core, although velocities specified by our best model (*AE09*) should be used if possible.

7.0 Conclusion

Using an Empirical Transfer Function method (AE2007), we have obtained stacked seismic record sections that reveal *S3KS* and *S4KS* phases with unusual clarity. Using these stacked sections, differential times for *S3KS*-*SKKS* and *S4KS*-*SKKS* are derived, providing the basis for precise determination of velocity structure in the outermost core. Over a wide range of mantle and core velocity models tested, the velocity at the top of the core is found to be V_o = 8.05±0.03 km/s. Our best fitting model for the outermost 200 km of the core (*AE09*) is compatible with uncertainties in Earth's gravity and moment of inertia, and agrees (to within less than one standard deviation) with the kinematics of well observed *PKP* and *PKIKP* core phases that were not used to construct our model. The similarity of all admissible outer core models to *PREM* in terms of velocity and velocity gradient suggest that its underlying assumptions of homogeneity and adiabaticity are valid. This argues against the presence of an anomalous layer at the top of the core, as suggested in some previous studies.

Acknowledgements

Figure (1a) was produced using GMT software (Wessel and Smith, 1998). Seismic Analysis Code software (Goldstein and Snoke, 2005) was used to filter the observed data. Data used for this study were obtained from the waveform archives of IRIS and POLARIS. The Associate Editor, George Helffrich is thanked for providing stimulating and useful discussions. Dr. Saturo Tanaka and an anonymous reviewer are thanked for providing constructive suggestions. This work was supported by NSERC Discovery Grant 194259-2005 RGPIN to DWE.

References

Aki, K., and Richards, P., 2002. Quantitative Seismology Second Edition. University Science Books, Sausalito, CA, 700 pp.

Alexandrakis, C., and Eaton, D. W., 2007. Empirical transfer functions: Application to determination of outermost core velocity structure using SmKS phases. Geophys. Res. Lett., 34: L22317 2007.

Buffett, B., Garnero, E. J., and Jeanloz, R., 2000. Sediments at the top of Earth's core. Science, 290: 1338-1342.

Chernick, M. R., 1999. Bootstrap Methods: A Practitioner's Guide. Wiley, New York, 264 pp.

Choy, G., 1977. Theoretical seismograms of core phases calculated by frequency-dependent full wave theory, and their interpretation. Geophys. J. R. Astron. Soc., 51: 275-312.

Crotwell, H. P., Owens, T. J., and Ritsema, J., 1999. The TauP toolkit; flexible seismic travel-time and ray-path utilities. Seis. Res. Lett., 70: 154-160.

Dziewonski, A. M., and Anderson, D. L., 1981. Preliminary Reference Earth Model. Phys. Earth Planet. Inter., 25: 297-356.

Eaton, D., and Kendall, M., 2006. Improving seismic resolution of outermost core structure by mulitchannel analysis and deconvolution of broadband *SmKS* phases. Phys. Earth Planet. Inter., 155: 104-119.

Fuchs K., and Müller, G., 1971. Computation of synthetic seismograms with the reflectivity method and comparison with observations. Geophys. J. R. Astron. Soc., 23: 417-433.

Garnero, E., and Helmberger, D., 1995. On seismic resolution of lateral heterogeneity in the Earth's outermost core. Phys. Earth Planet. Inter., 88: 117-130.

Garnero, E., Helmberger, D., and Grand, S., 1993. Constraining outermost core velocity with SmKS waves. Geophys. Res. Lett., 20: 2463-2466.

Goldstein, P., Snoke, A., 2005. "SAC Availability for the IRIS Community", Incorporated Institutions for Seismology Data Management Center Electronic Newsletter. http://www.iris.edu/news/newsletter/vol7no1/page1.htm

Hales, A., and Roberts, J., 1971. The velocities in the outer core. Bull. Seismol. Soc. Am., 61: 1051-1059.

Helffrich, G., and Kaneshima, S., 2004. Seismological constraints on Core Composition from Fe-O-S Liquid Immiscibility. Science, 306: 2239-2242.

Kennett, B.L.N., 1998. On the density distribution within the Earth. Geophys. J. Int., 132: 374-382.

Kennett, B. L. N., and Engdahl, E. R., 1991. Traveltimes for global earthquake location and phase identification. Geophys. J. Int., 105: 429-465.

Kennett, B. L. N., Engdahl, E. R., and Buland, R., 1995. Constraints on seismic velocities in the Earth from traveltimes. Geophys. J. Int., 122: 108-124.

Kennett, B. L. N., and Gudmundsson, O., 1996. Ellipticity corrections for seismic phases. Geophys. J. Int., 127: 40-48.

Koci, L., Belonoshko, A. B., and Ahuja, R., 2007. Molecular dynamics calculation of liquid iron properties and adiabatic temperature gradient in the Earth's outer core. Geophys. J. Int., 168: 890-894.

Langston, C., 1979. Structure under Mount Rainier, Washington, inferred from teleseismic body waves. J. Geophys. Res., 84: 4749-4762.

Lay, T., Hernlund, J., and Buffett, B. A., 2008. Core-mantle boundary heat flow. Nature Geoscience, 1: 25-32.

Lister, J. R., and Buffett, B. A., 1998. Stratification of the outer core at the core-mantle boundary. Phys. Earth Planet. Inter., 105: 5-19.

Mégnin, C., and Romanowicz, B., 2000. The shear velocity structure of the mantle from the inversion of body, surface and higher mode waveforms. Geophys. J. Int., 143: 709-728.

Morard, G., Sanloup, C., Guillot, B., Fiquet, G., Mezouar, M., Perrillat, J. P., Garbarino, G., Mibe, K., Komabayashi, T., and Funakoshi, K., 2008. In situ structural investigation of Fe-S-Si immiscible liquid system and evolution of Fe-S bond properties with pressure. J. Geophys. Res., 113: B10205.

Poirier, J. P., 2000. Introduction to the Physics of the Earth's Interior Second Edition. Cambridge University Press, Cambridge, 312 pp.

Sanloup, C., Fiquet, G., Gregoryanz, E., Morard, G., and Mezouar, M., 2004. Effects of Si on liquid Fe compressibility: Implications for sound velocity in core materials. Geophys. Res. Lett., 31: L07604.

Souriau, A., and Poupinet, G., 1991. A study of the outermost liquid core using differential travel times of the SKS, SKKS and S3KS phases. Phys. Earth Planet. Inter., 68: 183-199.

Souriau, A., Teste, A., and Chevrot, S., 2003. Is there any structure inside the liquid outer core? Geophys. Res. Lett., 30: 1567.

Tanaka, S., 2004. Seismic detectability of anomalous structure at the top of the Earth's outer core with broadband array analysis of *SmKS* phases. Phys. Earth Planet. Inter., 141: 141-152.

Tanaka, S., 2007. Possibility of a low *P*-wave velocity layer in the outermost core from global *SmKS* waveforms. Earth Planet. Sci. Lett., 259: 486-499.

Wessel, P., and Smith, W. H. F., 1998. New, improved version of the Generic Mapping Tools released. Eos Trans. AGU, 79: 579.

Williamson, E. D., and Adams, L. H., 1923. Density distribution in the Earth. J. Washington Acad. Sci., 13: 413-431.